



OPEN

Self-Assembly of Mesoporous Nanotubes Assembled from Interwoven Ultrathin Birnessite-type MnO₂ Nanosheets for Asymmetric Supercapacitors

Ming Huang¹, Yuxin Zhang^{1,2}, Fei Li¹, Lili Zhang³, Rodney S. Ruoff⁴, Zhiyu Wen² & Qing Liu¹

¹College of Materials Science and Engineering, Chongqing University, Chongqing 400044, P.R. China, ²National Key Laboratory of Fundamental Science of Micro/Nano-Devices and System Technology, Chongqing University, Chongqing 400044, P.R. China, ³Institute of Chemical and Engineering Sciences, A*STAR, 1 Pesek Road, Jurong Island 627833, Singapore, ⁴Department of Mechanical Engineering and the Materials Science and Engineering Program, The University of Texas at Austin, One University Station C2200, Austin, Texas 78712, United States.

Porous nanotubes comprised of MnO₂ nanosheets were fabricated with a one-pot hydrothermal method using polycarbonate membrane as the template. The diameter and thickness of nanotubes can be controlled by choice of the membrane pore size and the chemistry. The porous MnO₂ nanotubes were used as a supercapacitor electrode. The specific capacitance in a three-electrode system was 365 F g⁻¹ at a current density of 0.25 A g⁻¹ with capacitance retention of 90.4% after 3000 cycles. An asymmetric supercapacitor with porous MnO₂ nanotubes as the positive electrode and activated graphene as the negative electrode yielded an energy density of 22.5 Wh kg⁻¹ and a maximum power density of 146.2 kW kg⁻¹; these values exceeded those reported for other MnO₂ nanostructures. The supercapacitor performance was correlated with the hierarchical structure of the porous MnO₂ nanotubes.

With increasing demand for sustainable and renewable power sources in modern electronic industries, supercapacitors have attracted tremendous attention because of their high power density, excellent pulse charge-discharge characteristics, long cycling life and safe operation^{1–3}. Up to now, various materials, including carbonaceous materials^{4,5}, conducting polymers⁶, transition metal oxides/hydroxides^{7,8}, and hybrid composites^{9,10}, have been widely investigated as electrodes for supercapacitors. Compared to carbonaceous materials and conducting polymers, transition-metal oxides exhibit larger electrochemical capacitances and energy densities as they can provide a variety of oxidation states for efficient redox charge transfer which could satisfy the needs of high-performance supercapacitors. Hence, there has been extensive interest in developing the attractive transition metal oxide (such as MnO₂¹¹, Co₃O₄¹², NiO¹³, VO_x¹⁴, and CuO¹⁵) for supercapacitors.

In particular, manganese dioxide (MnO₂) has been extensively investigated as a supercapacitor electrode material due to its low cost, high natural abundance, high theoretical capacity (~1370 F g⁻¹), and non-toxicity^{11,16–20}. The electrochemical performance of MnO₂ has been found to be strongly influenced by a variety of factors including preparation conditions, particle size, morphology, and degree of crystallinity, and others. While nanosheets^{21,22}, hollow spheres²³, nanoflowers²⁴, nanowires/nanorods^{25–27}, thin films^{28,29}, and nanotubes^{30–32} have all been reported, the synthesis of MnO₂ with controllable particle size, morphology, and high crystallinity remained as a challenge. Among these structures, MnO₂ nanotubes can provide high surface area and a large surface-to-volume ratio to allow effective contact with the electrolyte ions, affording short ion diffusion paths and fast kinetics. The nanotube morphology can also accommodate large volume changes during the charge-discharge cycle and thereby improve the life of the electrode^{33,34}. Although significant research has been devoted to the synthesis of MnO₂ nanotubes, there was no effective method for the production of porous MnO₂ nanotubes with precise morphological control. Dong et al.³⁵ reported the synthesis of porous MnO₂/TiN nanotube coaxial arrays *via* a two-step procedure based on an electrodeposition process, while elegant, the process is also complicated and tedious. Zhu et al. prepared the porous MnO₂ nanotubes using a hydrothermal method coupled with post-treatment. But the thickness of the MnO₂ wall and the diameter of the nanotube are difficult to control³⁶. This motivated us to search for a simple way to prepare porous MnO₂ nanotube with controllable morphology.

SUBJECT AREAS:
ELECTROCHEMISTRY
SYNTHESIS AND PROCESSING

Received
24 October 2013

Accepted
6 January 2014

Published
27 January 2014

Correspondence and requests for materials should be addressed to Y.X.Z. (zhangyuxin@cqu.edu.cn); L.L.Z. (zhang_lili@ices.a-star.edu.sg) or Q.L. (qingliu@cqu.edu.cn)

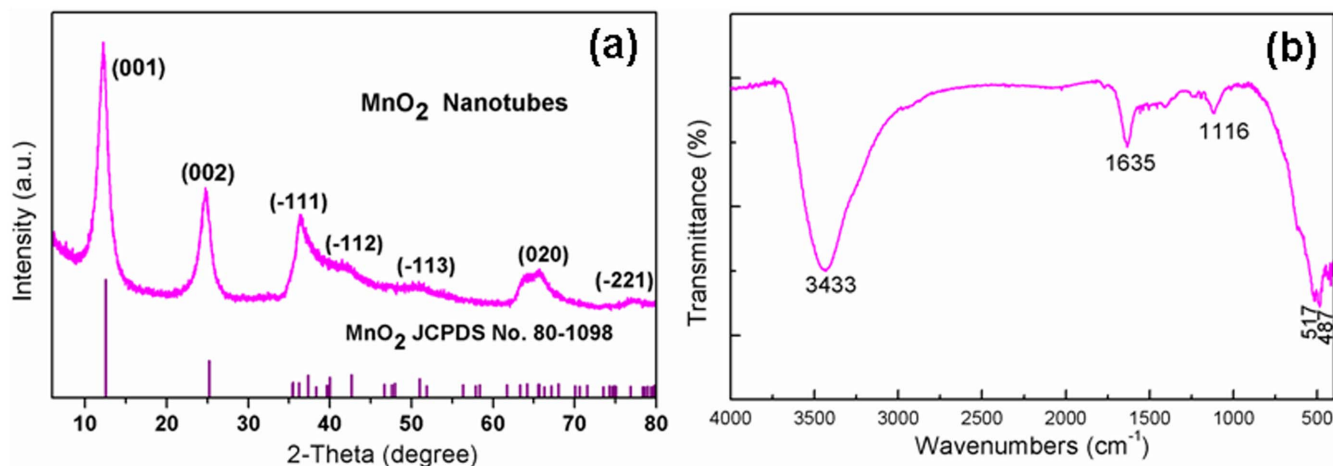


Figure 1 | (a) XRD pattern of nanotubes comprised of MnO₂ nanosheets. (b) FT-IR spectra of MnO₂ nanotubes.

In this work, we introduce a novel and effective one-step hydrothermal approach for the synthesis of porous MnO₂ nanotubes. The as-prepared MnO₂ nanotubes were porous and consisted of MnO₂ nanosheets with thickness of about 6 nm. The interconnected MnO₂ nanosheets in a mesoporous tubular structure can facilitate ion insertion/extraction and electron transport in the electrodes. An asymmetric supercapacitor with these porous MnO₂ nanotubes as the positive electrode and activated graphene as the negative electrode in 1 M Na₂SO₄ electrolyte had an energy density of 22.5 Wh kg⁻¹ with a maximum power density of 146.2 kW kg⁻¹.

Results

The morphology of MnO₂ nanotubes can be tailored by varying the pore size of the polycarbonate (PC) membrane, the concentration of Mn precursors, the processing temperature and the time. PC membranes with pore size of 200 nm, and a processing temperature of 140°C were investigated in this study (Figs. S1 and S2 showed the SEM images of the PC membrane). The structure and phase purity of the as-prepared MnO₂ samples were examined by X-ray powder diffraction (XRD, Figure 1a). The diffraction peaks at about 12.5°, 25.2° and 37° from the as-prepared 200-nm diameter MnO₂ nanotubes matched the standard XRD pattern of birnessite-type manganese

oxide crystal (JCPDS 80-1098, $a = 5.149 \text{ \AA}$, $b = 2.843 \text{ \AA}$, $c = 7.716 \text{ \AA}$). No other peaks that would be associated with another phase or impurity were observed. Fourier transform infrared spectroscopy (FT-IR) was used to characterize the functionality of MnO₂ nanotubes and the results were shown in Figure 1b. The main absorption bands were found at 3433, 1635, 1116, 517, and 487 cm⁻¹, respectively. The broad band around 3433 cm⁻¹ represented the O-H stretching of the inter-layer water molecules, while the weak band at 1635 cm⁻¹ was probably due to the bending vibrations of the O-H groups from the adsorbed water molecules^{37,38}. The absorption peak at 1116 cm⁻¹ was attributed to the -OH bending vibrations combined with Mn atoms. The peaks at 517 and 487 cm⁻¹ were the main characteristic absorption bands of birnessite, corresponding to Mn-O stretching modes of the octahedral layers in the birnessite structure which was consistent with the previous XRD result.

An illustration of the formation of MnO₂ nanotubes was shown in Figure 2a. The MnO₂ nuclei were firstly formed in a short time and adsorbed on the surface of the polycarbonate³⁹. As the hydrothermal reaction further proceeded, Ostwald ripening process⁴⁰ took place, in which the smaller particles were consumed while the bigger ones grew into nanosheets with a lamellar structure^{41,42}. Subsequently, the nanosheets were self-assembled into porous MnO₂ nanotubes

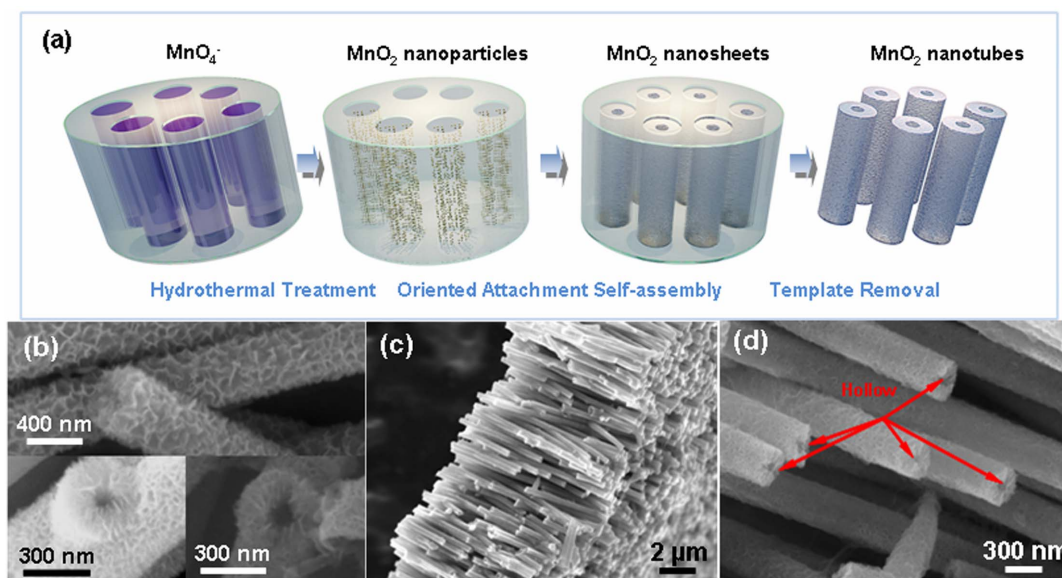


Figure 2 | (a) Schematic illustration of the procedure to synthesize porous MnO₂ nanotubes. SEM images of MnO₂ nanotubes. (b) Detailed images of the MnO₂ nanotubes. (c) Side-view of MnO₂ nanotubes arrays. (d) Enlarged view of the MnO₂ nanotubes arrays.



due to the “oriented attachment” and “self-assembly” processes⁴⁰, which involved a spontaneous self-organization^{43,44} of the adjacent nanosheets.

Scanning electron microscope (SEM) images (Figure 2b–2d; see also Fig. S3) revealed that the average diameter of the MnO₂ nanotubes was about 200 nm, which is coincided with the average pore diameter of the original polycarbonate (PC) membrane. However, the length of the MnO₂ nanotubes ranged from 4 to 8 μm, which was shorter than the thickness of the PC membrane (Fig. S2). The length of the MnO₂ nanotubes was not uniform due to the fracture during the removal of the PC template. All the nanotubes were made of MnO₂ nanosheets. Each nanotube had flaky appearance, and the assembly of ultrathin nanosheets into interconnected porous structure provided large and open active area. The porous and hollow nanotubes were further elucidated by Transmission electron microscopy (TEM, Figure 3). High-resolution TEM (HRTEM, Figure 3b and c) images of the nanosheets clearly showed that the birnessite-type MnO₂ nanostructures were crystallized with the interplanar distance of 0.253 and 0.212 nm, corresponding to the (200) and (−112) plane of the birnessite-type MnO₂, respectively^{41,42,45}. The interplanar spacing of MnO₂ nanosheet is 0.7 nm, corresponds to the typical interplanar spacing of the (001) plane of birnessite-type MnO₂ that prefers forming two-dimensional flaky structures. The corresponding selected area electron diffraction (SAED) pattern of the nanosheet edge exhibited polycrystalline nature of birnessite-type MnO₂. The lattice fringes attributing to the (200), (−112), and (020) planes were clearly visible, in agreement with the XRD results. Nitrogen adsorption-desorption results (see Supplementary Fig. S3) indicated that the MnO₂ nanotubes had a Brunauer-Emmett-Teller (BET) surface area of 85.2 m² g^{−1} with a pore volume of 0.394 cm³ g^{−1}. The pore size distribution obtained from the adsorption branch by the Barrett-Joyner-Halenda (BJH) method indicated that the average pore size was ~18 nm. The mesopore-in-nanotubular hierarchical morphology with controlled porous structures were advantageous for enhanced electrochemical capacitors applications since large specific surface area and open mesoporous tubular structures provided effective active sites for the chemical reactions, shortened the ion diffusion paths and facilitated rapid ion transport.

To evaluate the potential applications as the electrode materials for supercapacitor, the electrochemical properties of mesoporous MnO₂ nanotubes were firstly studied in a three-electrode system in 1 M Na₂SO₄ and the results were shown in Figure 4. The almost symmetric rectangular shape of the CV curves (Figure 4a) and the near linear symmetric triangular charge-discharge plots (Figure 4b) showed reversible and capacitive behavior of the MnO₂ nanotubes-based electrode. The specific capacitance of the electrode was calculated from the galvanostatic discharge curve using the following equation:

$$C = \frac{I \Delta t}{m \Delta V}$$

where C (F g^{−1}) is the specific capacitance, I (A) is the constant discharge current, Δt (s) is the discharge time, ΔV (V) is the potential window, and m (g) is the mass of the active material in the electrode. The specific capacitance of the MnO₂ nanotubes was 365 F g^{−1} at the current density of 0.25 A g^{−1}; this value exceeded many MnO₂ electrodes in previous reports (Table S1)^{41,46–54}. The corresponding volumetric capacitance of the total electrode including the current collector (Ni foam) was estimated to be about 107.4 ± 3 F cm^{−3} according to the thickness (68 ± 2 μm) of the compressed MnO₂/Ni foam electrode. Furthermore, we have measured the electrochemical properties of two reference samples (commercial MnO₂ and MnO₂ nanosheets obtained without PC template) for comparison (Fig. S5). According to the discharge time from the charge/discharge curves (Fig. S5d), the as-prepared MnO₂ nanotubes show a much higher specific capacitance than the commercial MnO₂ (14.3 F g^{−1}) and MnO₂ nanosheets (194.5 F g^{−1}). The results show that the MnO₂ nanotubes are a promising candidate for the electrode materials for supercapacitors. The enhanced capacitive performance can be attributed to 1) the hierarchical-mesoporous nanotubular structure facilitated the ion insertion/extraction; and 2) the interconnected porous ultrathin MnO₂ nanosheets cannot only shorten the ion diffusion paths, but also ensure a high utilization of the active materials (since the redox reaction was surface reaction only and the bulk metal oxide did not contribute). The specific capacitance of MnO₂ nanotubes electrode at various current densities was shown in Figure 4c. When the current density was increased from 0.25 to 10 A g^{−1}, the specific capacitance can still be as high as 202.7 F g^{−1} (decreased about 45%), indicating the good rate capability of the MnO₂ nanotubes.

The Nyquist plots of MnO₂ nanotubes electrode before and after 3000 cycles were obtained using AC electrochemical impedance spectroscopy (EIS) in the frequency range from 100 kHz to 0.01 Hz at open circuit potential by applying an AC voltage with 5 mV amplitude. The Nyquist plots in Figure 4d were composed of one semicircle in the high-frequency region and a linear part in the low-frequency region, which illustrated typical capacitor behavior. The contact resistances of the MnO₂ electrodes (before and after 3000 cycles) were 1.6 and 2.0 Ω, respectively, indicating good conductivity of the electrolyte and assembly of the cell. The equivalent circuit for the Nyquist plots was shown as an inset in Figure 4c (see Supplementary Table S2 for simulation result). After 3000 cycles, only a slight increase of the charge transfer resistance (R_{ct}) from 3.9 to 7.4 Ω was observed.

Figure 4e showed the long-term cycling performance of the MnO₂ electrode by galvanostatic charge-discharge process at the current density of 5 A g^{−1} for consecutive 3000 cycles. The specific capacitance

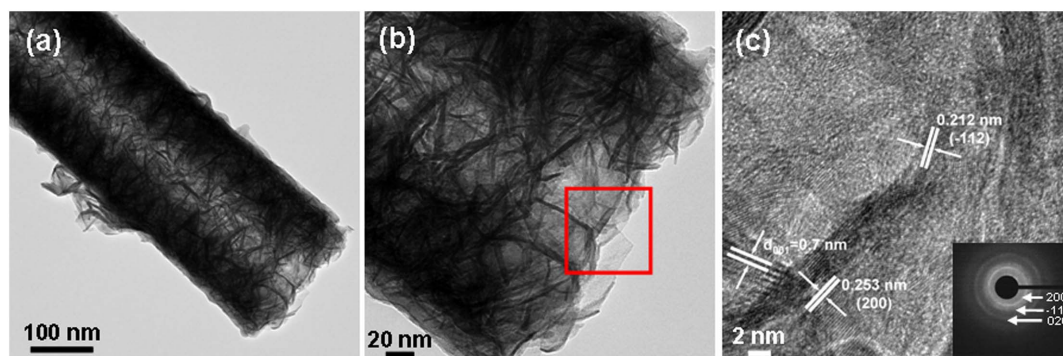


Figure 3 | (a) Low-magnification TEM image of an individual porous MnO₂ nanotube. (b) Detailed images of the terminal nanosheets of the MnO₂ nanotube. (c) HRTEM image of the MnO₂ nanosheets (the red boxed region in (b)). Bottom-right inset is the corresponding SAED pattern.

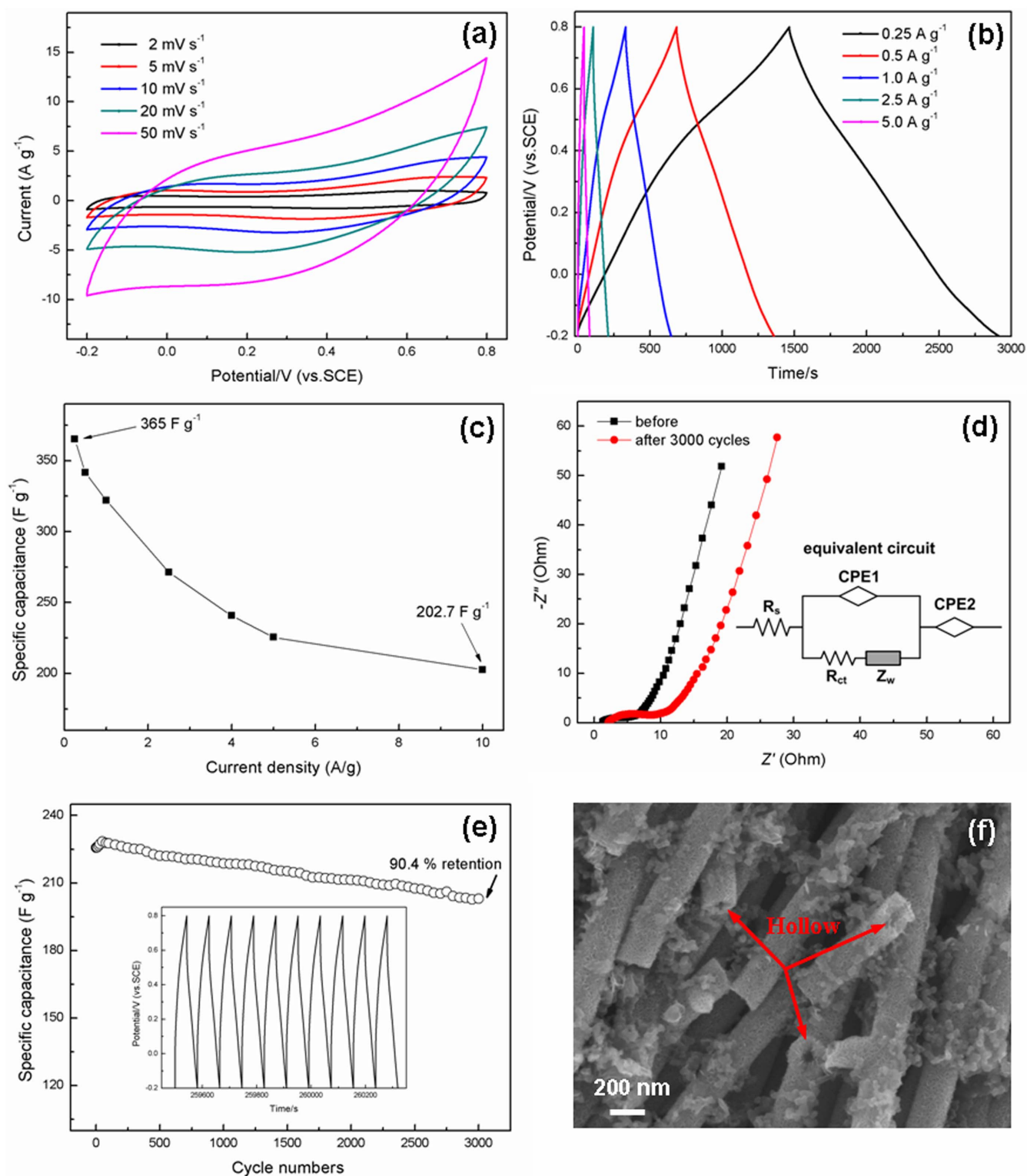


Figure 4 | (a) Cyclic voltammograms of MnO₂ nanotubes in a 1 M Na₂SO₄ aqueous electrolyte. (b) Charge-discharge curves of MnO₂ nanotubes at different current densities. (c) Specific capacitance of MnO₂ nanotubes measured under different current densities. (d) Electrochemical impedance spectrum of the MnO₂ nanotubes electrodes at open circuit potential in the frequency range from 0.01 Hz to 100 kHz. The inset shows the equivalent circuit. (e) Cycling performance of MnO₂ nanotubes at the current density of 5 A g⁻¹. The inset shows the charge-discharge curves of the last 10 cycles of the MnO₂ nanotubes electrode. (f) The corresponding SEM image of the electrode after 3000 electrochemical cycles.

of the MnO₂ nanotube-based electrode maintained about 90.4% of its initial value after 3000 cycles, demonstrating the good stability of the MnO₂ nanotubes as a supercapacitor's electrode. In addition, the charge-discharge curves of the last 10 cycles were shown as the inset

in Figure 4e. The similar symmetric triangular charge-discharge curves (as comparing to the initial curve) indicated no significant structural change of the MnO₂ nanotubes electrode during the charge/discharge processes. Meanwhile, the SEM images of the MnO₂ nanotubes



electrode before and after 3000 cycles were investigated (see Supplementary Fig. S6). The SEM image of the MnO₂ nanotube electrode after electrochemical cycles in Figure 4f suggested that the hierarchical porous nanotube structure was maintained rather well. The unique porous hollow nanostructure may resolve the aggregation problem and can accommodate the volume expansion of the electrode materials during long-term cycles, which was beneficial for the structural stability of the MnO₂ electrodes. The crystalline structure change of the MnO₂ nanotubes electrode after charge/discharge cycles at the current density of 1 A g⁻¹ was examined through XRD. As shown in Figure S7, the interplanar spacing of MnO₂ increases slightly after the charge process (diffraction peaks are at a smaller degree), and then decreases during the following discharge (diffraction peaks at higher degree). After 3000 cycles, the crystallinity of MnO₂ was relatively well maintained which can be ascribed to small structural expansion/contraction occurring during charge/discharge cycles. The XRD results further demonstrated the good stability of the MnO₂ nanotubes for high-performance supercapacitors.

An asymmetric supercapacitor was fabricated using the MnO₂ nanotubes as the positive electrode and the activated graphene (AG) as the negative electrode with 1.0 M Na₂SO₄ aqueous electrolyte (Figure 5a). The SEM images and the electrochemical properties of the AG were shown in Figure S8 and S9 (see Supplementary Information). In the design cell, the mass ratio of the positive electrode (0.7 mg) to the negative electrode (1.3 mg) was fixed at 0.5 on the basis of the specific capacitance values and the potential windows of the two materials. The asymmetric device exhibited capacitive behavior with nearly rectangular-shaped CV curves without obvious redox peaks with the operating voltage up to 2.0 V (Figure 5b). Figure 5c showed the typical CV curves of the asymmetric cell in the voltage window from 0 to 1.8 V at the scan rates of 5, 10, 20, 50 and 100 mV s⁻¹. The CV profile of the asymmetric cell remained relatively rectangular at a high scan rate of 100 mV s⁻¹, which demonstrated good charge/discharge properties and rate capability of the asymmetric supercapacitor.

Discussion

The galvanostatic charge-discharge curves at various current densities were shown in Figure 5d. It can be seen that the potentials of the charge-discharge lines are nearly proportional to the charge or discharge time, indicating a rapid I–V response, small equivalent series resistance (ESR) and ideal capacitive characteristics. The EIS results (see Supplementary Fig. S10) of the asymmetric supercapacitor before and after 10000 cycles test confirmed the relative small change in the ESR. From the slope of the discharge curve, the gravimetric capacitance (*C_t*) of the asymmetric supercapacitor was 50 F g⁻¹ based on the total mass of active materials in the two electrodes at a current density of 0.25 A g⁻¹. A maximum gravimetric energy density and power density of 22.5 Wh kg⁻¹ and 146.2 kW kg⁻¹ were obtained (Figure 5e), respectively, based on the total weight of the electrodes (i.e. mass of MnO₂ + AG). The values are not only higher than most of the MnO₂-based supercapacitors^{41,55–67} but also comparable to those MnO₂-based composite supercapacitors^{68–70} (see Supplementary Table S3 for detailed comparison). According to the fascinating synergetic properties or multifunctionalities of components^{71,72}, we can design a smart hybrid architecture based on mesoporous MnO₂ nanotubes with conductive supports or other metal oxide/hydroxide, and further improve the energy density of the MnO₂ nanotubes-based supercapacitors. The asymmetric supercapacitor device achieved a volumetric energy density and power density of 7.2 Wh L⁻¹ and 46.8 kW L⁻¹, respectively, based on the total electrode (i.e. mass of MnO₂ + AG + Ni foam) density of 4.0 g cm⁻³ (Table S3). In addition, the performance of the fully packaged asymmetric cell was also estimated (Table S4). The packaged device showed a maximum practical gravimetric energy density of 1.2 Wh kg⁻¹ (highest power density of 7.5 kW kg⁻¹) and volumetric energy

density of 5.0 Wh L⁻¹ (highest power density of 31.5 kW L⁻¹). We connected our prototype device to a red LED and successfully lighted it (Figure 5f). More importantly, the LED was on for about 120 seconds after being charged for 27 s at 1.8 V (see Supplementary Movie S1). The device retained 76.3% of its initial specific capacitance after 10000 cycles (see Supplementary Fig. S11 and S12). In addition, the SEM images of MnO₂ nanotubes-based electrode in the asymmetric supercapacitor device after 10000 cycles revealed that the hierarchical porous MnO₂ nanotubes structure was well maintained (see Supplementary Fig. S13). These results showed our MnO₂ nanotubes//AG asymmetric supercapacitor device is promising in practical applications.

In summary, hierarchical and porous MnO₂ nanotubes comprised of ultrathin nanosheets have been prepared by a one-step hydrothermal treatment using PC as the template. The unique mesopore-in-nanotubular structure facilitated fast ion transport and the ultrathin MnO₂ nanosheet shortens the ion diffusion paths and ensured high utilization of the active material. The specific capacitance of the MnO₂ nanotubes-based electrode was 365 F g⁻¹ at a current density of 0.25 A g⁻¹ with capacitance retention of 90.4% retention after 3000 cycles in a three-electrode cell system. An asymmetric supercapacitor based on MnO₂ nanotubes as the positive electrode and AG as the negative electrode in aqueous electrolyte in a fully packaged cell was fabricated. The device can be reversibly charged and discharged at an operation voltage of 1.8 V in 1.0 M Na₂SO₄ aqueous electrolyte, delivering an energy density of 22.5 Wh kg⁻¹ and a maximum power density of 146.2 kW kg⁻¹. The results indicated that the mesoporous MnO₂ nanotube is a promising candidate in electrochemically stable supercapacitors for practical applications. Such unique nanosheets-built MnO₂ nanotubes might also be used in broad fields including dye wastewater treatment and gas sensors. Furthermore, the proposed synthetic methodology would open new opportunities of other transition metal oxides for high-performance supercapacitors.

Methods

Materials. All the chemical reagents were purchased from Alfa Aesar, which are of analytical purity and used without any further purification. The polycarbonate (PC) membrane filters (Whatman 110606; pore diameter: 200 nm) were used for the fabrication of mesoporous MnO₂ nanotubes.

Preparation of nanotubes comprised of MnO₂ nanosheets. Prior of being used, the PC substrate was treated by hydrochloric acid (1 M) to remove the impurities on the surface of PC. The MnO₂ nanotubes were prepared in KMnO₄ solution using the PC as the template. In a typical synthetic procedure, the treated PC membrane was immersed in KMnO₄ solution (0.02 M; 30 mL) under ultrasonication for 20 minutes. The mixture (including the PC membrane) was transferred into a Teflon-lined stainless steel autoclave which was subsequently maintained at 140 °C for 24 h. The MnO₂/PC membrane composite was then taken out from the solution and dissolved away PC in dichloromethane to obtain pure MnO₂ sample. Finally, the MnO₂ sample was washed with distilled water and ethanol, and dried at 60 °C to obtain the porous MnO₂ nanotubes.

Electrochemical measurements. A three-electrode system was used to measure the response of the MnO₂ nanotubes as the working electrode using 1 M Na₂SO₄ aqueous solution as the electrolyte, with a platinum plate as the counter electrode and saturated calomel electrode (SCE) as the reference electrode, respectively. The working electrode was prepared by mixing 70 wt% active material (MnO₂ nanotubes), 20 wt% acetylene black and 10 wt% polyvinylidene fluoride (PVDF) in N-methyl-2-pyrrolidone (NMP) and the slurry was spread onto a foam nickel current collector (1 × 1 cm²). The electrode was heated at 120 °C for 12 h to evaporate the solvent and then uniaxially pressed under 10 MPa. The electrode contained 2 mg of active materials (MnO₂ nanotubes alone).

The asymmetric supercapacitor was measured with a two-electrode system, including two slices of electrode material with the same size, a Whatman filter paper as separator, and two pieces of nickel foil as the current collectors. In the two-electrode system, MnO₂ nanotubes were the positive electrode, and activated graphene (AG) mixed with 20 wt% acetylene black and 10 wt% polyvinylidene fluoride (PVDF) in N-methyl-2-pyrrolidone (NMP) to form a paste and then pressed into uniform sheet was the negative electrode. The two electrodes were assembled together with Whatman filter paper soaked in 1 M Na₂SO₄ solution before being connected to the potentiostat. The electrochemical performance in both three-electrode and two-electrode configurations were carried out on the CHI 660E electrochemical station.

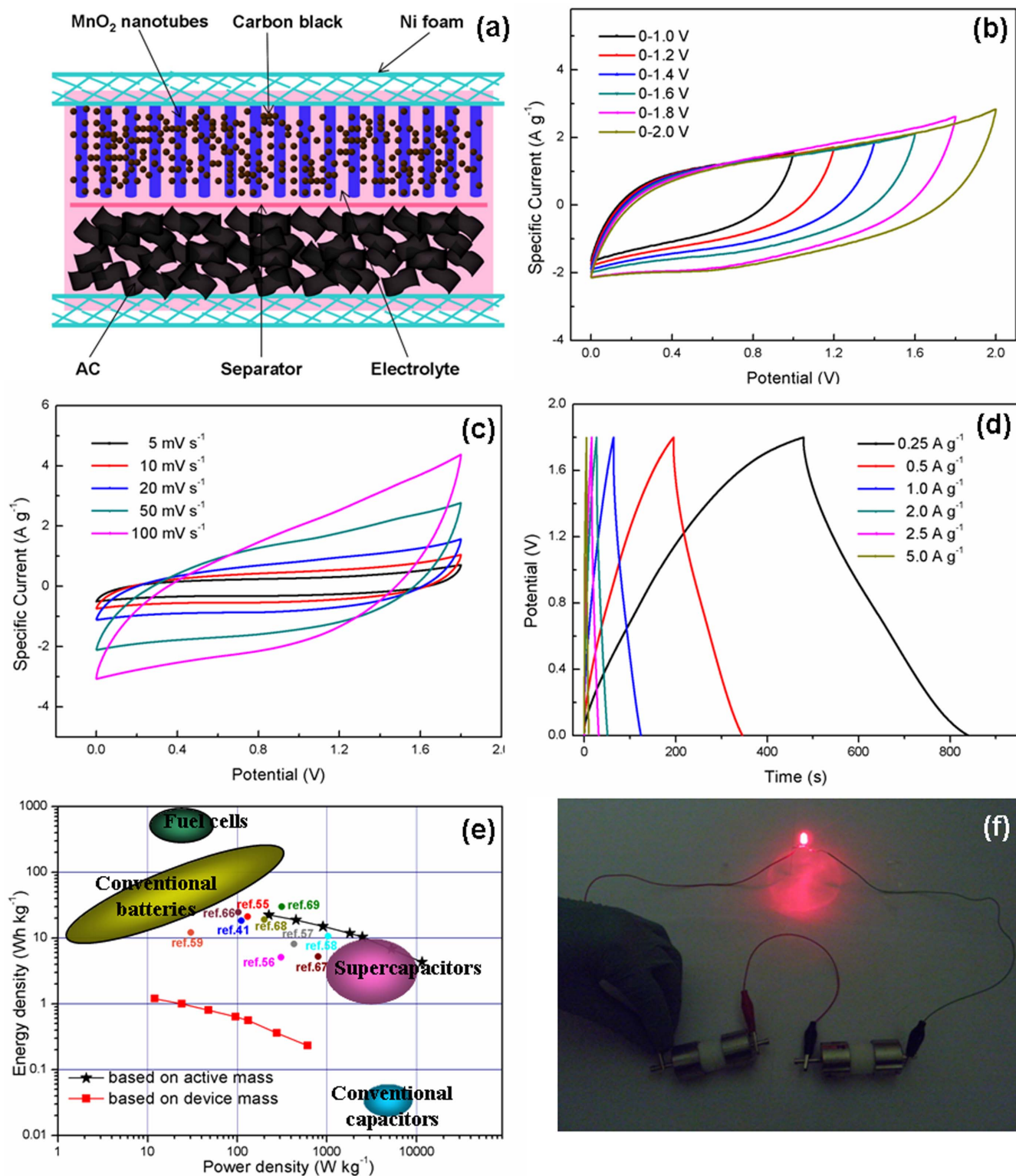


Figure 5 | (a) Schematic illustration of the asymmetric supercapacitor configuration. (b) CV curves of MnO₂ nanosheets-bulit nanotubes//AG asymmetric supercapacitor measured at different potential window at a scan rate of 50 mV s⁻¹. (c) CV curves of the asymmetric supercapacitor measured at different scan rates from 0 and 1.8 V. (d) Galvanostatic charge-discharge curves at different current densities. (e) The energy density vs. power density of the MnO₂ nanotubes//AG asymmetric supercapacitor in a Ragone plot for fuel cells, conventional batteries, conventional capacitors, and ultracapacitors. (f) Digital image of a red-light-emitting diode (LED) lighted by the MnO₂ nanotubes//AG device.

The cyclic voltammetry (CV) and galvanostatic charge-discharge techniques were employed to investigate the electrochemical performance of the electrodes. All the operating current densities were calculated based on the mass of active materials (mass of MnO₂ nanotubes for three-electrode system and the total weight of

MnO₂ nanotubes with AG for two-electrode system). The electrochemical impedance spectroscopy (EIS) was conducted in the frequency range between 100 kHz and 0.01 Hz with a perturbation amplitude of 5 mV versus the open-circuit potential.



1. Miller, J. R. & Simon, P. Materials science - Electrochemical capacitors for energy management. *Science* **321**, 651–652 (2008).
2. Simon, P. & Gogotsi, Y. Materials for electrochemical capacitors. *Nat. Mater.* **7**, 845–854 (2008).
3. Liu, C., Li, F., Ma, L.-P. & Cheng, H.-M. Advanced materials for energy storage. *Adv. Mater.* **22**, E28–E62 (2010).
4. Chaikittisilp, W., Ariga, K. & Yamauchi, Y. A new family of carbon materials: synthesis of MOF-derived nanoporous carbons and their promising applications. *J. Mater. Chem. A* **1**, 14–19 (2013).
5. Chaikittisilp, W. *et al.* Nanoporous carbons through direct carbonization of a zeolitic imidazolate framework for supercapacitor electrodes. *Chem. Commun.* **48**, 7259–7261 (2012).
6. Ermis, E., Yigit, D. & Gullu, M. Synthesis of poly(N-alkyl-3,4-dihydrothieno 3,4-b 1,4 oxazine) derivatives and investigation of their supercapacitive performances for charge storage applications. *Electrochim. Acta* **90**, 623–633 (2013).
7. Hu, M., Ishihara, S. & Yamauchi, Y. Bottom-up synthesis of monodispersed single-crystalline cyano-bridged coordination polymer nanoflakes. *Angew. Chem. Int. Ed.* **52**, 1235–1239 (2013).
8. Ji, J. *et al.* Nanoporous Ni(OH)₂ thin film on 3D ultrathin-graphite foam for asymmetric supercapacitor. *ACS Nano* **7**, 6237–6243 (2013).
9. Yang, Y. *et al.* Vapor phase polymerization deposition of conducting polymer/graphene nanocomposites as high performance electrode materials. *ACS Appl. Mater. Interfaces* **5**, 4350–4355 (2013).
10. Bastakoti, B. P. *et al.* Mesoporous carbon incorporated with In₂O₃ nanoparticles as high-performance supercapacitors. *Eur. J. Inorg. Chem.* **2013**, 1109–1112 (2013).
11. Zhao, X. *et al.* Incorporation of manganese dioxide within ultraporous activated graphene for high-performance electrochemical capacitors. *ACS Nano* **6**, 5404–5412 (2012).
12. Xia, X.-H., Tu, J.-P., Wang, X.-L., Gu, C.-D. & Zhao, X.-B. Mesoporous Co₃O₄ monolayer hollow-sphere array as electrochemical pseudocapacitor material. *Chem. Commun.* **47**, 5786–5788 (2011).
13. Zhang, Y. Q. *et al.* Self-assembled synthesis of hierarchically porous NiO film and its application for electrochemical capacitors. *J. Power Sources* **199**, 413–417 (2012).
14. Qu, Q., Zhu, Y., Gao, X. & Wu, Y. Core-shell structure of polypyrrole grown on V₂O₅ nanoribbon as high performance anode material for supercapacitors. *Adv. Energy Mater.* **2**, 950–955 (2012).
15. Dubal, D. P., Gund, G. S., Holze, R. & Lokhande, C. D. Mild chemical strategy to grow micro-roses and micro-woolen like arranged CuO nanosheets for high performance supercapacitors. *J. Power Sources* **242**, 687–698 (2013).
16. Wei, W., Cui, X., Chen, W. & Ivey, D. G. Manganese oxide-based materials as electrochemical supercapacitor electrodes. *Chem. Soc. Rev.* **40**, 1697–1721 (2011).
17. Li, Q. *et al.* Design and synthesis of MnO₂/Mn/MnO₂ sandwich-structured nanotube arrays with high supercapacitive performance for electrochemical energy storage. *Nano Lett.* **12**, 3803–3807 (2012).
18. Chen, K., Noh, Y. D., Li, K., Komarneni, S. & Xue, D. Microwave-hydrothermal crystallization of polymorphic MnO₂ for electrochemical energy storage. *J. Phys. Chem. C* **117**, 10770–10779 (2013).
19. Kang, J. *et al.* Enhanced supercapacitor performance of MnO₂ by atomic doping. *Angew. Chem. Int. Ed.* **52**, 1664–1667 (2013).
20. Zhang, Y. X., Huang, M., Li, F., Wang, X. L. & Wen, Z. Q. One-pot synthesis of hierarchical MnO₂-modified diatomites for electrochemical capacitor electrodes. *J. Power Sources* **246**, 449–456 (2014).
21. Zhang, Y. *et al.* Crystallization design of MnO₂ towards better supercapacitance. *CrystEngComm* **14**, 5892–5897 (2012).
22. Kai, K. *et al.* Electrochemical characterization of single-layer MnO₂ nanosheets as a high-capacitance pseudocapacitor electrode. *J. Mater. Chem.* **22**, 14691–14695 (2012).
23. Tang, X., Liu, Z.-h., Zhang, C., Yang, Z. & Wang, Z. Synthesis and capacitive property of hierarchical hollow manganese oxide nanospheres with large specific surface area. *J. Power Sources* **193**, 939–943 (2009).
24. Su, M. *et al.* Three-dimensional nanoflower-like MnO₂ functionalized graphene as catalytically promoted nanolabels for ultrasensitive electrochemiluminescence immunoassay. *Electrochim. Acta* **97**, 333–340 (2013).
25. Wei, C. *et al.* Two-dimensional beta-MnO₂ nanowire network with enhanced electrochemical capacitance. *Sci. Rep.* **3**, 2193 (2013).
26. Yu, M. *et al.* Manganese dioxide nanorod arrays on carbon fabric for flexible solid-state supercapacitors. *J. Power Sources* **239**, 64–71 (2013).
27. Lu, X. *et al.* Facile synthesis of large-area manganese oxide nanorod arrays as a high-performance electrochemical supercapacitor. *Energy Environ. Sci.* **4**, 2915–2921 (2011).
28. Yan, D. *et al.* MnO₂ film with three-dimensional structure prepared by hydrothermal process for supercapacitor. *J. Power Sources* **199**, 409–412 (2012).
29. Yang, D. Pulsed laser deposition of manganese oxide thin films for supercapacitor applications. *J. Power Sources* **196**, 8843–8849 (2011).
30. Xiao, W., Xia, H., Fuh, J. Y. H. & Lu, L. Growth of single-crystal alpha-MnO₂ nanotubes prepared by a hydrothermal route and their electrochemical properties. *J. Power Sources* **193**, 935–938 (2009).
31. Li, L., Nan, C., Lu, J., Peng, Q. & Li, Y. Alpha-MnO₂ nanotubes: high surface area and enhanced lithium battery properties. *Chem. Commun.* **48**, 6945–6947 (2012).
32. Luo, J. *et al.* Synthesis of single-crystal tetragonal alpha-MnO₂ nanotubes. *J. Phys. Chem. C* **112**, 12594–12598 (2008).
33. Yan, W. *et al.* Mesoporous manganese oxide nanowires for high-capacity, high-rate, hybrid electrical energy storage. *ACS Nano* **5**, 8275–8287 (2011).
34. Chen, S., Zhu, J., Wu, X., Han, Q. & Wang, X. Graphene oxide-MnO₂ nanocomposites for supercapacitors. *ACS Nano* **4**, 2822–2830 (2010).
35. Dong, S. *et al.* One dimensional MnO₂/titanium nitride nanotube coaxial arrays for high performance electrochemical capacitive energy storage. *Energy Environ. Sci.* **4**, 3502–3508 (2011).
36. Zhu, J. *et al.* Oxidation-etching preparation of MnO₂ tubular nanostructures for high-performance supercapacitors. *ACS Appl. Mater. Interfaces* **4**, 2769–2774 (2012).
37. Yao, W., Zhou, H. & Lu, Y. Synthesis and property of novel MnO₂@polypyrrole coaxial nanotubes as electrode material for supercapacitors. *J. Power Sources* **241**, 359–366 (2013).
38. Huang, Y., Lin, Y. & Li, W. Controllable syntheses of alpha- and delta-MnO₂ as cathode catalysts for zinc-air battery. *Electrochim. Acta* **99**, 161–165 (2013).
39. Bechelany, M., Amin, A., Brioude, A., Cornu, D. & Miele, P. ZnO nanotubes by template-assisted sol-gel route. *J. Nanopart. Res.* **14**, 1–7 (2012).
40. Zeng, H. C. Ostwald ripening: A synthetic approach for hollow nanomaterials. *Curr. Nanosci.* **3**, 177–181 (2007).
41. Zhang, X. *et al.* Rapid hydrothermal synthesis of hierarchical nanostructures assembled from ultrathin birnessite-type MnO₂ nanosheets for supercapacitor applications. *Electrochim. Acta* **89**, 523–529 (2013).
42. Zhou, J. *et al.* Novel synthesis of birnessite-type MnO₂ nanostructure for water treatment and electrochemical capacitor. *Ind. Eng. Chem. Res.* **52**, 9586–9593 (2013).
43. Fang, X. S. *et al.* Direct observation of the growth process of MgO nanoflowers by a simple chemical route. *Small* **1**, 422–428 (2005).
44. Wang, F. *et al.* Manganese oxides with rod-, wire-, tube-, and flower-like morphologies: highly effective catalysts for the removal of toluene. *Environ. Sci. Technol.* **46**, 4034–4041 (2012).
45. Liu, J. *et al.* Co₃O₄ nanowire@MnO₂ ultrathin nanosheet core/shell arrays: a new class of high-performance pseudocapacitive materials. *Adv. Mater.* **23**, 2076–2081 (2011).
46. Yeager, M. *et al.* Highly efficient K_{0.15}MnO₂ birnessite nanosheets for stable pseudocapacitive cathodes. *J. Phys. Chem. C* **116**, 20173–20181 (2012).
47. Ming, B. *et al.* Microwave-hydrothermal synthesis of birnessite-type MnO₂ nanospheres as supercapacitor electrode materials. *J. Power Sources* **198**, 428–431 (2012).
48. Dubal, D. P., Dhawale, D. S., Salunkhe, R. R. & Lokhande, C. D. A novel chemical synthesis of Mn₃O₄ thin film and its stepwise conversion into birnessite MnO₂ during super capacitive studies. *J. Electroanal. Chem.* **647**, 60–65 (2010).
49. Munaiah, Y., Raj, B. G. S., Kumar, T. P. & Ragupathy, P. Facile synthesis of hollow sphere amorphous MnO₂: the formation mechanism, morphology and effect of a bivalent cation-containing electrolyte on its supercapacitive behavior. *J. Mater. Chem. A* **1**, 4300–4306 (2013).
50. Kundu, M. & Liu, L. Direct growth of mesoporous MnO₂ nanosheet arrays on nickel foam current collectors for high-performance pseudocapacitors. *J. Power Sources* **243**, 676–681 (2013).
51. Sopic, S., Peter, R., Petravic, M. & Mandic, Z. New insights into the mechanism of pseudocapacitance deterioration in electrodeposited MnO₂ under negative potentials. *J. Power Sources* **240**, 252–257 (2013).
52. Song, Z. *et al.* A facile template-free synthesis of alpha-MnO₂ nanorods for supercapacitor. *J. Alloys Compd.* **560**, 151–155 (2013).
53. Li, W. *et al.* MnO₂ ultralong nanowires with better electrical conductivity and enhanced supercapacitor performances. *J. Mater. Chem.* **22**, 14864–14867 (2012).
54. Xia, H., Feng, J., Wang, H., Lai, M. O. & Lu, L. MnO₂ nanotube and nanowire arrays by electrochemical deposition for supercapacitors. *J. Power Sources* **195**, 4410–4413 (2010).
55. Qu, Q. T. *et al.* A new cheap asymmetric aqueous supercapacitor: activated carbon//NaMnO₂. *J. Power Sources* **194**, 1222–1225 (2009).
56. He, Y. *et al.* Freestanding three-dimensional graphene/MnO₂ composite networks as ultra light and flexible supercapacitor electrodes. *ACS Nano* **7**, 174–182 (2013).
57. Cottineau, T., Toupin, M., Delahaye, T., Brousse, T. & Belanger, D. Nanostructured transition metal oxides for aqueous hybrid electrochemical supercapacitors. *Appl. Phys. A* **82**, 599–606 (2006).
58. Chen, C.-Y., Fan, C.-Y., Lee, M.-T. & Chang, J.-K. Tightly connected MnO₂-graphene with tunable energy density and power density for supercapacitor applications. *J. Mater. Chem.* **22**, 7697–7700 (2012).
59. Bahloul, A. *et al.* Polypyrrole-covered MnO₂ as electrode material for supercapacitor. *J. Power Sources* **240**, 267–272 (2013).
60. Yu, G. *et al.* Solution-processed graphene/MnO₂ nanostructured textiles for high-performance electrochemical capacitors. *Nano Lett.* **11**, 2905–2911 (2011).
61. Jaidev, Jafri, R. I., Mishra, A. K. & Ramaprabhu, S. Polyaniline-MnO₂ nanotube hybrid nanocomposite as supercapacitor electrode material in acidic electrolyte. *J. Mater. Chem.* **21**, 17601–17605 (2011).
62. Deng, L. *et al.* Graphene-MnO₂ and graphene asymmetrical electrochemical capacitor with a high energy density in aqueous electrolyte. *J. Power Sources* **196**, 10782–10787 (2011).



63. Sun, Z., Firdoz, S., Yap, E. Y.-X., Li, L. & Lu, X. Hierarchically structured MnO₂ nanowires supported on hollow Ni dendrites for high-performance supercapacitors. *Nanoscale* **5**, 4379–4387 (2013).
64. Wu, T.-H., Chu, Y.-H., Hu, C.-C. & Hardwick, L. J. Criteria appointing the highest acceptable cell voltage of asymmetric supercapacitors. *Electrochem. Commun.* **27**, 81–84 (2013).
65. Xu, C., Du, H., Li, B., Kang, F. & Zeng, Y. Asymmetric activated carbon-manganese dioxide capacitors in mild aqueous electrolytes containing alkaline-earth cations. *J. Electrochem. Soc.* **156**, A435–A441 (2009).
66. Lei, Z., Zhang, J. & Zhao, X. S. Ultrathin MnO₂ nanofibers grown on graphitic carbon spheres as high-performance asymmetric supercapacitor electrodes. *J. Mater. Chem.* **22**, 153–160 (2012).
67. Wang, Y.-S., Tsai, D.-S., Chung, W.-H., Syu, Y.-S. & Huang, Y.-S. Power loss and energy density of the asymmetric ultracapacitor loaded with molybdenum doped manganese oxide. *Electrochim. Acta* **68**, 95–102 (2012).
68. Wu, Z.-S. *et al.* High-energy MnO₂ nanowire/graphene and graphene asymmetric electrochemical capacitors. *ACS Nano* **4**, 5835–5842 (2010).
69. Fan, Z. *et al.* Asymmetric supercapacitors based on graphene/MnO₂ and activated carbon nanofiber electrodes with high power and energy density. *Adv. Funct. Mater.* **21**, 2366–2375 (2011).
70. Gao, H., Xiao, F., Ching, C. B. & Duan, H. High-performance asymmetric supercapacitor based on graphene hydrogel and nanostructured MnO₂. *ACS Appl. Mater. Interfaces* **4**, 2801–2810 (2012).
71. Chen, H. *et al.* One-step fabrication of ultrathin porous nickel hydroxide-manganese dioxide hybrid nanosheets for supercapacitor electrodes with excellent capacitive performance. *Adv. Energy Mater.* (2013) DOI: 10.1002/aenm.201300580.
72. Chen, H., Zhou, S., Chen, M. & Wu, L. Reduced graphene oxide–MnO₂ hollow sphere hybrid nanostructures as high-performance electrochemical capacitors. *J. Mater. Chem.* **22**, 25207–25216 (2012).

Acknowledgments

The authors gratefully acknowledge the financial supports provided by National Natural Science Foundation of China (Grant no. 51104194), Doctoral Fund of Ministry of Education of China (20110191120014), No. 43 Scientific Research Foundation for the Returned Overseas Chinese Scholars, National Key laboratory of Fundamental Science of Micro/Nano-device and System Technology (2013MS06, Chongqing University), State Education Ministry and Fundamental Research Funds for the Central Universities (Project no. CDJZR12248801, CDJZR12135501, and CDJZR13130035, Chongqing University, PR China).

Author contributions

Y.X.Z., L.L.Z. and Q.L. conceived and designed the experiments. M.H. and F.L. prepared self-assembled nanostructures and the supercapacitor electrodes, and conducted the electrochemical measurements. Z.Y.W. helped with TEM and electrochemical measurements and initial studies. R.S.R. helped with modification of manuscripts and kind discussion on details. Y.X.Z., Z.Y.W. and Q.L. wrote the manuscript. All the authors commented on the manuscript.

Additional information

Supplementary information accompanies this paper at <http://www.nature.com/scientificreports>

Competing financial interests: The authors declare no competing financial interests.

How to cite this article: Huang, M. *et al.* Self-Assembly of Mesoporous Nanotubes Assembled from Interwoven Ultrathin Birnessite-type MnO₂ Nanosheets for Asymmetric Supercapacitors. *Sci. Rep.* **4**, 3878; DOI:10.1038/srep03878 (2014).



This work is licensed under a Creative Commons Attribution-NonCommercial-NoDerivs 3.0 Unported license. To view a copy of this license, visit <http://creativecommons.org/licenses/by-nc-nd/3.0>